

ULTRASONIC TOMOGRAPHY OF  
PERSPEX / POLYSTYRENE COMPOSITES

by

MOHID.FARHAN MANZOOR.

TH  
NET/1999/M  
M3194



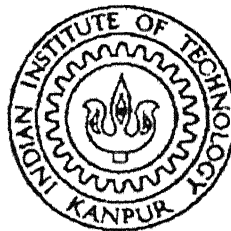
# ULTRASONIC TOMOGRAPHY OF PERSPEX / POLYSTYRENE COMPOSITES

*A Thesis Submitted  
in Partial Fulfilment of the Requirements  
for the Degree of*

Master of Technology

by

MOHD.FARHAN MANZOOR



NUCLEAR ENGINEERING AND TECHNOLOGY PROGRAMME  
INDIAN INSTITUTE OF TECHNOLOGY , KANPUR

July, 1999

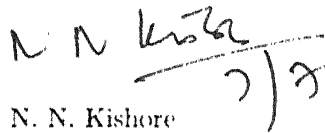
21 OCT 1999  
CENTRAL LIBRARY  
I. I. T., KANPUR

**A 129574**



# CERTIFICATE

It is certified that the work contained in the thesis entitled, "Ultrasonic Tomography of Perspex/polysterene composites" by Mohd. Farhan Manzoor, has been carried out under my supervision and this work has not been submitted elsewhere for a degree.



Dr. N. N. Kishore

Professor

Department of Mechanical Engg.

IIT Kanpur

DEDICATED TO  
my  
BELOVED PARENTS

## Abstract

The present investigation involves ultrasonic tomographic non-destructive evaluation of composite specimens implanted with artificial inclusions of polystyrene in perspex and evaluation of effectiveness of different features of ultrasonic signal in detecting different types of flaws.

Four different specimens are used which are made of perspex and the inclusions are of polystyrene. The wedge is used only for the normal incidence of the ultrasonic ray so that the transmission through the specimen is maximum. A through-transmission technique is used for data collection. The test section is immersed in the water which act as a couplant. After collecting the data for the required number of rays and views and applying correction is given as the input to the Convolution Back Projection algorithm. The data is reconstructed with different class of filters such as cosine, sinc, hamming and Ramachandran-Lakshminarayan.

The output of the reconstruction algorithm after pseudo colouring is an image which show clearly the different acoustic impedences zones. So flaws can easily be detected.

The results are quite encouraging. The present experimental set-up, after some modification, can be used for detailed flaw detection and sizing in 3-Dimensional ultrasonic tomography.

# Acknowledgement

I would like to express my deep felt sincere gratitude and appreciation to my thesis supervisor Dr. N.N.Kishore and Dr. P.Munshi for the skillful guidance, constant supervision, timely suggestions in carrying out the present work.

I am grateful to my family members for constantly encouraging me throughout my thesis work.

I would like to thank project associates Pankaj and Amit for helping me in coding and research scholars Rathore ji and Singhal ji in performing the experiments.

I would like to thank all the members of house number 520, IIT Kanpur for providing me the home made delicious foods and a homely environment.

Finally I express thanks to my younger brother Rehan and friends, Manish ji, Vinay, Tariq Bhai, Kshitiz, Nasir, Rahul, Ghulam(Gulli), Yusuf, Ruchi, Mathur, Ankur, Kamlesh who made my stay here a memorable and enjoyable one.

# Nomenclature

$f$	function representing the spatial distribution of any physical quantity
$x, y$	cartesian coordinates
$r, \phi$	polar coordinates
$p$	line integral data (projection data)
$N$	energy of the acoustic waave after travelling a distance $dl$
$N_0$	initial energy of the acoustic wave
$\mu$	slowness coefficient
$\wedge$	Fourier transform
$R$	Fourier frequency
$R_c$	cut-off frequency
$W$	window function
$W''(0)$	second order derivative of window function
$E_1$	inherent error due to finite cut-off
$\nabla^2$	Laplacian
$NRAY$	number of scans per view
$NANGLE$	number of views

$v(x, y)$       Velocity of the propagating wave.

# List of Figures

2.1	Parallel Beam Data Collection Geometry . . . . .	18
3.1	Schematic Diagram of Ultrasonic Setup . . . . .	25
3.2	Photographic view of the Ultrasonic Setup . . . . .	26
3.3	Specimen 1 . . . . .	30
3.4	Specimen 2 . . . . .	30
3.5	Specimen 3 . . . . .	31
3.6	Specimen 4 . . . . .	31
3.7	Wedge . . . . .	32
4.1	$1/N$ MAX plot for simulated specimens . . . . .	42
4.2	$1/N$ MAX plot for simulated specimens . . . . .	42
4.3	Original Image for the simulated specimen 1 . . . . .	43
4.4	Reconstructed Image with h54 and h99 filters . . . . .	43
4.5	Original Image for the simulated specimen 2 . . . . .	44
4.6	Reconstructed Image with h54 and h99 filters . . . . .	44
4.7	Original Image for the simulated specimen 3 . . . . .	45
4.8	Reconstructed Image with h54 and h99 filters . . . . .	45
4.9	Original Image for the simulated specimen 4 . . . . .	46

4.10	Reconstructed Image with h54 and h99 filters . . . . .	46
5.1	1/NMAX plot for real specimens . . . . .	53
5.2	1/NMAX plot for real specimens . . . . .	53
5.3	Original Image for the specimen 1 . . . . .	54
5.4	Reconstructed Image with h54 and h99 filters . . . . .	54
5.5	Original Image for the specimen 2 . . . . .	55
5.6	Reconstructed Image with h54 and h99 filters . . . . .	55
5.7	Original Image for the specimen 3 . . . . .	56
5.8	Reconstructed Image with h54 and h99 filters . . . . .	56
5.9	Original Image for the specimen 4 . . . . .	57
5.10	Reconstructed Image with h54 and h99 filters . . . . .	57

# List of Tables

4.1	Filter details . . . . .	37
4.2	Summary of results for simulated specimen 1 . . . . .	41
4.3	Summary of results for simulated specimen 2 . . . . .	41
4.4	Summary of results for simulated specimen 3 . . . . .	41
4.5	Summary of results for simulated specimen 4 . . . . .	41
5.1	Summary of results for Specimen 1 . . . . .	52
5.2	Summary of results for specimen 2 . . . . .	52
5.3	Summary of results for specimen 3 . . . . .	52
5.4	Summary of results for specimen 4 . . . . .	52

# Contents

Certificate	3
Acknowledgement	ii
Nomenclature	iii
List of Figures	viii
List of Tables	x
Abstract	i
<b>1 Introduction</b>	<b>1</b>
1.1 Image Reconstruction from Projections . . . . .	2
1.2 An Overview of the process of CT . . . . .	2
1.3 Composite Materials . . . . .	2
1.4 Nondestructive Testing . . . . .	3
1.5 Ultrasonic Testing . . . . .	4
1.5.1 Presentation of ultrasonic data . . . . .	6
1.6 Reconstruction Algorithms . . . . .	6
1.7 Ultrasonic Tomography . . . . .	7

1.8	Literature Review . . . . .	9
1.8.1	Experimental Techniques . . . . .	9
1.8.2	Acoustic Tomography . . . . .	13
1.9	Thesis Layout . . . . .	15
<b>2</b>	<b>Theoretical Formulation</b>	<b>16</b>
2.1	Preliminaries . . . . .	16
2.2	Data Collection Mode . . . . .	17
2.3	The CBP Algorithm . . . . .	17
<b>3</b>	<b>Experimental Set-up and Procedure</b>	<b>23</b>
3.1	Present Set-up . . . . .	23
3.2	Components of Experimental Set-up . . . . .	24
3.3	Specimen Preparation . . . . .	28
3.4	Experimental Procedure . . . . .	32
<b>4</b>	<b>Data Analysis</b>	<b>34</b>
4.1	Numerical Implementation of the Programme for Discrete Data . . . . .	34
4.2	Programme for Simulating Data . . . . .	35
4.3	Programme for Reconstruction . . . . .	35
4.4	Programme for Displaying Reconstructed Image and Colour Levels . . . . .	37
4.5	Colour Code . . . . .	37
4.6	Validation of CBP from Simulated Data . . . . .	39
<b>5</b>	<b>Experimental results and Discussion</b>	<b>47</b>
5.1	Data Used . . . . .	47
5.2	Discussion of the Results . . . . .	49
5.3	Comparative Study of Filters . . . . .	50



# Chapter 1

## Introduction

The technique of computerised tomography (CT) has established itself as a leading tool in diagnostic radiology over the past twenty years and it is gaining importance in the nondestructive evaluation area in a variety of situations. In conventional projection radiography, the result is obtained just in the form of a shadowgraph requiring subtle interpretation. CT, however, uses tomographic reconstruction to combine the information from multiple projections. Thus, the CT information is displayed quantitatively as a reconstructed slice plane of the object and it can provide accurate quantitative measures of material characteristics in small volume elements of the component.

It is noted that tomographic extensions of classical measurement techniques incorporate multiple projections, which increases the data collection time. The results, however, are much better if tomographic reconstruction is used. Tomography, if perfected, can also provide a cross validation of other experimental techniques.

## 1.1 Image Reconstruction from Projections

The range of applicability of image reconstruction is very wide. At one end data from electron microscope are used to reconstruct the molecular structure of bacteriophages, while at the other end, data collected by the rockets sent outside the earth's atmosphere are used to reconstruct the X-ray structure of supernova remnants. Of all the applications, probably the greatest effect on the world at the largest has been in the area of diagnostic medicine.

Image reconstruction can be very aptly defined in words of Herman(1980) as:

“ Image reconstruction from projections in the process of producing an image of a two-dimensional distribution (usually of some physical property) from estimates of its line integrals along a finite number of lines of known locations”.

## 1.2 An Overview of the process of CT

The aim of computerized tomography (CT) is to obtain information regarding the nature of the material occupying exact positions inside the object. there are other modes of traditional tomography, e.g. line tomography and transaxial tomography. In tradition form of tomography, objects which are out of focal plane are visible on the image, although in a blurred form. In CT, the images of cross-section are not influenced by the objects outside those sections.

## 1.3 Composite Materials

Demand imposed by modern advanced technologies on materials have become so diverse and severe that they often cannot be met by single component conventional materials. It is necessary to combine two or more materials to make a composite to meet the demand.

Constituents not only contribute their respective share, but their combined action transcends the sum of the individual properties and provides new performance, unattainable by constituents acting alone. Composites can be formally defined as materials having two or more chemically distinct materials or phases with clear interfaces on a macroscale among them.

The fibre reinforced materials are probably the most important class of composite materials which are used widely in structural applications particularly when weight saving is crucial. These materials offer high strength-to-weight and modulus-to-weight ratios apart from their properties of excellent corrosion resistance, formability and mechanical properties which can be controlled to significant degree.

## 1.4 Nondestructive Testing

Since man and their machines are fallible, there is a need to inspect the components to assess the material. A wide variety of test schemes exist, some destructive and some non-destructive. The practical benefits of nondestructive testing are obvious by its name, as long as the results are reliable and the inspection is cost-effective. In general, the various nondestructive evaluation (NDE) techniques can be placed into two categories: active and passive. The active techniques are those where something is introduced into or onto the specimen and a response is expected if a defect is present whereas passive techniques are those that monitor or observe the item during either a typical load environment or a proof cycle and attempt to determine the presence of a defect through some reaction of the specimen. Magnetics, ultrasonics, radiography fall in the category of active NDE and acoustic emission, noise analysis, leak testing etc. are the examples of passive NDE.

## 1.5 Ultrasonic Testing

Ultrasonic inspection involves introducing a low energy, high frequency stress pulse into the material under inspection and examining the subsequent propagation of this energy. Defects such as cracks and inclusions act as a source of wave scattering through reflection, refraction, diffraction and mode conversion. It will be quite relevant at this stage to have a brief discussion on different types of waves.

A wave is a transient phenomenon that depends upon time and position in space and which transports energy through space. The effect of a wave due to interaction with matter may be measured by certain physical attributes such as displacement, strain, stress, density, electric field, magnetic field etc. In case of mechanical waves, it is convenient to classify them according to the geometry of the medium through which the wave is propagating. Thus, bulk waves are those that propagate through a medium so large in size compared to the wavelength that the medium may be considered to be infinite. Bulk waves are generally plane or spherical waves depending on the shape of the wave front.

Bulk waves in solids are normally described as being longitudinal (or compressional or dilatational) as the particle displacement caused at the points are parallel to the direction in which the wave is propagating. Sound waves in atmosphere is an example of this. A transverse (or shear) wave is one which produce particle displacements that are perpendicular to the direction of the wave propagation. Longitudinal waves typically travel at a faster speed than transverse waves.

Surface or Rayleigh waves are observed in the vicinity of the boundary when bulk waves propagate parallel to the boundary in a semi-infinite solid medium. Its velocity is less than that of transverse waves in the same medium and it attenuates rapidly on entering the medium. The particle displacement produced by the passing of this wave is such that the path described by the particle over one complete cycle of the wave is an ellipse. These waves can be suitably used to detect surface flaws.

The interaction of bulk waves with geometrical constraints (in the form of a stress free parallel boundary, e.g., a plate) produces a very complicated structure of waves referred to as plate waves or Lamb waves. Lamb waves are of two types, symmetric and antisymmetric. In symmetric type, the particle displacement fields are symmetric with respect to the plate midplane and quite analogous to longitudinal modes. The lamb waves, in general, are composed of two components; standing waves, that exist between the top and bottom surfaces of the plate and travelling waves, that propagate parallel to the midplane.

For the present concern, the stress waves are generally assumed to be in the ultrasonic range, i.e., having frequencies greater than 20KHz. When an ultrasonic wave reaches an interface or a discontinuity, a portion of the energy is reflected and the other portion is transmitted. The amount of the reflected energy depends on the relative acoustic impedances of the media. Thus, the energy transmitted through the material is reduced due to attenuations in the sample. Subsequently, these variations are reflected as the change in the relevant ultrasonic feature and serve as means for locating defects or discontinuities in the path of the wave.

In practice, elastic waves are generated through the excitation of a peizoelectric device (in the probe) by electric pulse generator and the mechanical energy is then fed into the test specimen using a coupling medium (couplant) such as water, oil, grease etc.

Depending on the mode of recieving of the waveform, testing are performed, in general, either in pulse-echo or in through-transmission mode. In pulse-echo mode of scanning, a high voltage spike sets the probe into oscillation and it becomes an open non-conducting electrical circuit and the reciever circuit waits for the return signal to strike the probe. In the through-transmission arrangement, the sending and the receiving end probes have different electronic circuits. Through-transmission is effective for detecting delamination , voids etc. In this case, however, both sides of the specimen should be

accessible. Pulse-echo technique can be employed if the part is not very thin, so that the initial pulse and the reflected pulse from the back surface do not overlap, nor the specimen is too thick, causing excessive attenuation by high signal loss even for defect free results.

### **1.5.1 Presentation of ultrasonic data**

Historically, investigators have used the terminology A, B, C-scan to describe the type of presentation of the data taken during ultrasonic study of specimens. An A-scan indicates a variation of signal amplitude at a point with time, where the ordinate of the oscilloscope trace is proportional to the amplitude and abscissa to the time elapsed. A B-scan is the presentation of the data in the form of a depth profile versus position along a cross section. A C-scan is the presentation of variation of any feature or feature set as a function of position of the transducer in two dimensionals relative to the surface of the examined specimen. During automated scanning, the transducer is generally translated along two mutually perpendicular axes in raster fashion using stepper motors. Essentially feature or feature set, used to construct the C-scan, is extracted from the recieved ultrasonic waveform obtained in the A-scan mode. Another recent way of representing ultrasonic data is by using tomographic technique which reconstructs a slice of an object from multiple projections. Thus, tomography, if perfected, can provide better results

## **1.6 Reconstruction Algorithms**

The simplifying assumptions in setting up the theory for reconstruction algorithms are

1. Slices are infinitely thin
2. For any perticular source and detector pair position, wave travel in the same straight line (which lies in the infinitely thin slice).

A consequence of the first assumption is that the distinction between the voxel and the pixel disappears. Indeed, since the slice is infinitely thin, it can be thought of as a picture whose gray level or the colour level at any point  $(x, y)$  is proportional to the relative slowness coefficient  $\mu(x, y)$  at that point. This is the reason why the theory behind reconstruction algorithm is referred to as "*image reconstruction from projections*". Tomographic algorithms can be classified into two categories:

1. Transform methods
2. Series expansion methods

When the set of data available is large and complete, transform methods are generally used. Whereas if the data set is not complete, series expansion methods are preferred. Transform methods are direct methods while series expansion methods can be direct as well as iterative. The scope of the transform algorithm is limited to the reconstruction of a two-dimensional (2-D) image from integrals along a line in the plane, but they are useful in many application involving three-dimensional (3-D) objects because such object can be decomposed into a stack of thin 2-D slices. If line integral data are available for each of these individual slices independent of others, then the 3-D reconstruction problem may be decomposed into repeated 2-D reconstruction of serial cross-sections of the object.

## 1.7 Ultrasonic Tomography

Although CT was conceived originally for X-rays, in recent times, CT has been implemented successfully for other energy sources such as acoustic, laser, microwaves etc. Among these, acoustic tomography (especially using ultrasonic waves (UCT)), has special importance in application to NDE. Like X-ray CT, the physics of ultrasonic CT involves two steps:

1. The measurement of the time-of-flight data for the wave passing through a number

of different paths through a test object, followed by

2. The reconstruction of slowness coefficient values at all interior points from the data collected in step (1).

Thus, acoustical tomography can be defined as a technique to determine values of a spatially varying acoustic parameter of interest across a slice through an object. Waves travel through the sample (from a series of source locations) to receivers at appropriate positions around the object. The source and the receiver locations are chosen such that the rays pass through as large a fraction of the object volume as possible. The relative positioning of the source and receiver should also conform to any requirement for regular positioning in the reconstruction procedure. As the source and the detector are moved around the object, a number of individual projections (or measured data sets) are obtained. Each projection is composed of a transmitted intensity pattern which depends on the path concerned. After completing a scan consisting of a number of projections, the distribution of the slowness coefficients within the object is reconstructed by one of the several reconstruction techniques.

The major problem in applying UCT is that ultrasound does not travel strictly in linear fashion and suffers scattering, ray bending and the diffraction at the interface of any dissimilar material. In medical applications, however, UCT can be used safely in soft tissues imaging where deviation from linearity in propagation is minimal. Among industrial applications, practical material characterisation problem such as study of residual stress distribution has also been tackled by UCT. With proper guideline for collecting projection data and proper modification in the reconstruction technique, accurate quantitative evaluation of the material properties of the object slice can be accomplished.

## 1.8 Literature Review

Nondestructive testing and evaluation (NDE) of composite materials poses a challenge to both researchers and applied technologist. Ultrasonic methods, however, are most common and practice widely because of the low cost, relative ease in their use and the amount of information that can be obtained from them. In this section, a state-of-the-art review of the ultrasonic methods for NDE of composite materials is presented. This survey covers experimental techniques in nondestructive application of ultrasonics to characterize them and detect different flaw/damage found in them.

### 1.8.1 Experimental Techniques

A comprehensive review article on ultrasonic NDE of advanced composite was presented by Henneke [1990]. The article covers a wide range of works, applied to composite materials, which include different modes of wave propagation, material characterization, attenuation measurement, C-scan techniques, ultrasonic spectroscopy.

The most basic application of ultrasonics is in characterizing any material by measuring the velocity of wave in it. Such well known techniques of calculating wave speed by measuring time-of-flight, are described in Bray and Stanley [1989] and Krautkramer and Krautkramer [1990]. A wave pulse is established at one surface of the material by a transmitting transducer. A second receiving transducer is located at the far side of the material to receive the signal after travelling through one thickness of the specimen. This mode of operation is called pitch-catch method. In the other method, called pulse-echo technique, the same transmitting transducer may be shutdown momentarily and the signal is received after travelling through twice the thickness of the specimen. In both the cases time-of-flight is measured and subsequently the wave speed is computed.

Wave speeds, in different modes, can be directly correlated with the material prop-

erties and vice-versa ( Kolsky [1963]). In isotropic materials, two independent velocity measurements are enough to determine the complete elastic moduli. The attenuation of any ultrasonic wave propagating through a medium gives in the information about the state in quantity of the medium. Attenuation is one of the main characteristics of a propagating wave that is highly dependent on the material and its properties.

Tanchert and Hsu [1973] studied attenuation measurement of glass/fibre reinforced unidirectional and cross piled composite laminates under cyclically applied tension and compression loads. The attenuation increased with time but did not get back to its initial loading upon unloading. Attenuation was noted to be frequency dependent, increasing with higher frequencies and vice-versa.

Store and Clarke [1975] observed that the main factors influencing ultrasonic attenuation were delamination, voids and state of the cure of the resin. Fibre volume fraction did not influence attenuation much. They performed C-scan on fabricated panels and attenuation was measured by comparing the originals with and without the specimen in the water bath. The attenuation was considered as the total loss and back faces end that associated with the propagation through the specimen.

Hayford et al [1977] and Meron et al [1977] established a correlation between ultrasonic attenuation and failure strength in composite specimen.

Meron et al [1977] concluded that ultrasonic attenuation is a more sensitive indicator of the degradation of the properties due to exposure of the specimen in the hot water.

Hayford and Henneke [1979] presented the results of a model to find attenuation changes observed (in real time) in tension test of graphite/epoxy specimens. They concluded that more transverse cracks do not occur in piles if the crack density with some minimum saturation spacing is reached. The changes in attenuation depends on the spacing of the transverse cracks which acts as a diffraction grating for the passage of the ultrasonic beam.

Williams and Doll [1980] measured the ultrasonic attenuation in graphite/epoxy specimens that were subjected to compression-compression fatigue. A through-transmission mode was adapted and, for measuring attenuation, the amplitude of the received pulse was compared with that of the input pulse at four narrow band centre frequencies of 0.5, 1.0, 1.5 and 2.0 MHz. They also noted that attenuation to be frequency dependent. Group velocity, however, was found to be frequency independent.

Srivastava and Prakash [1987] measured attenuation in glass fibre zirconia hybrid composite by through-transmission immersion technique using a pair of 10 MHz probes. Attenuation was measured by comparing the amplitude of transmitted probe with that of the incident probe. The result showed a bilinear relationship to be existent between pre-fatigue ultrasonic attenuation and the fatigue life.

As defined earlier, a C-scan is the presentation of variation of the ultrasonic attenuation of features(s) as a function of the transducer in two dimensions relative to the surface of the examined specimen. More recent developments in C-scan the various imaging techniques to improve data presentation. Multiple thresholds are set and either various shades of gray or different colours are assigned to the different threshold levels.

Hagemaijer et al [1970,1971] inspected boron, glass and graphite reinforced polymer matrix composites using ultrasonic C-scan. They observed that through transmission techniques had the advantage of not being affected by surface roughness, surface contour etc. They also noted penetration at higher frequencies to be inadequate. However, 1.0, 2.25 and 5.0 MHz were suitable for through transmission. They found that the C-scan was quite effective for locating planar defects and suggested that reference specimen with built in discontinuities were essential to perform correct inspection.

Mool and Stephenson [1971] inspected boron/epoxy with known defects, using through-transmission ultrasonic C-scan with infocused probes. They found it necessary to perform scans with different amplification and threshold levels to display all artifacts. They

observed that complete loss of a through-transmission original was typical of a delamination or air void. With higher setting of the threshold, they observed that even normal signal had considerable fluctuations. Ultrasonic C-scan has also been used to study damage initiator and development in composites (Sturgeon [1977], Nahas [1985]).

In recent years attenuation has been given to the development of automated C-scan technique. With the advent of composite materials, requirements have emerged for the development of the new inspection procedures. Mahoon et al [1982] discussed how the necessity of a skilled personnel and the variability of the personal judgement was overcome by automatic scanning system developed by British Aerospace. The scanning system has facility of manipulating probes in an water-squirter system that controlled data collection and analysis.

C-scans of tubular graphite epoxy specimen used in aerospace industries were performed by Rogovsky [1985]. In this investigation, flaws were simulated in different layers of tube and a method called "multiple reflections" was suggested where the number and amplitude of multiple reflection (from the boundary of the bonds) were considered. He concluded that an optimal selection of the sequence and number of signals for the flaw detectors gating yielded good detectability of the simulated flaws.

Preuss and Clark [1988] used time-of-flight (TOF) ultrasonic C-scan for detection, sizing and characterization of defects in carbon/fibre composite components. They obtained the depth wise information by recording the position of the defect echoes in time on the A-Scan. The C-Scan was constructed by using this TOF information rather than the back wall echo amplitude. They, however, applied the technique on 56-ply thick carbon/fibre composite panel with damage from impact and fatigue loading.

Miller [1990] summarised a quantitative ultrasonic nondestructive technique applied to evaluate impact damage and porosity in graphite/epoxy composite laminates. Quantitative imaged based on the slope of the attenuation coefficient measured as the function

of frequency over a broad bandwidth were obtained using a phase insensitive acousto-electric receiving transducer. Low velocity impact yielded increased values for the slope of the attenuation.

### 1.8.2 Acoustic Tomography

Computed tomography (CT) in particular X-ray CT, is a powerful NDE tool that has seen a rapid development in the past two decades. CT uses Computer reconstruction to combine the information obtained from multiple projections. The quantitative CT information is displayed as a reconstructed slice plane of the part. Thus, in addition to qualitative evaluation, the CT data values can provide accurate quantitative measurement of material characteristics (density) in small volume elements of the object.

Although CT is relatively new, most of its mathematical basis traces its origin to the pioneering work of Radon [1917] and his work on the reconstruction of functions from the line integral data in the early part of the century. He showed that internal information of a three dimensional object (represented by a mathematical function) could be determined from the values of a set of line integrals of the mathematical functions. This work was expanded to radiography by Cormack [1963]. His work included both the mathematical approach and experimental verification. However, it remained until the invention of CT scanner by Hounsfield [1973], for the technique to be practically useful.

Kak [1979] reviewed the major developments in imaging with computed tomography using X-ray, emission and ultrasound sources. The background and theory of the CT systems, types and applications of the CT systems can be found in the book by Herman [1980].

D.P.Jansen et al [1994] used Lamb wave tomography for finding out damages in advanced composite laminates. They studied two thin film laminate samples consisted of 16 layers of carbon-fibre reinforced epoxy with a quasi isotropic lay-up configuration and

had been previously loaded in a biaxial test method until failure. The resulting damage, in the form of fibre failure, matrix cracking and delamination, has been imaged using a novel Lamb wave immersion tomography techniques. Images created with this method were correlated with images obtained with C-scan techniques. Both C-scan and Lamb wave tomography were able to identify clearly regions of damage in the two samples.

William Wright et al [1997] studied an entirely air-coupled inspection system using a pair of micro machined silicon capacitance transducers to image defects in the plates of different materials (0.7 mm to 2.22 mm thickness) using air-coupled Lamb wave tomography. Filter back projection algorithm was used in a form of difference tomography to reconstruct images of defects upto 10 mm diameter machined in aluminium and perspex plates, as well as in samples of carbon fibre reinforced polymer (CFRP). The technique was able to resolve non-central defects as well as multiple flaws within the scan area.

D.P. Jansen and D.A. Hutchins [1991] utilized ultrasonic Rayleigh and Lamb waves to reconstruct tomographic images of defects within metallic samples they used through immersion techniques, Rayleigh waves were used for the identification of surface structures on thick samples, while Lamb waves are used to detect structures in thin sheets, they obtained tomographic images which gives information concerning the location and nature of the defects.

D.P. Jansen et al [1993] obtained ultrasonic tomographic images from objects of rectangular cross section by scanning spring-loaded transducers across the sample phases. The complete system was under the control of the microcomputer, resulting in a entirely automatic data collection system. Selected images obtained from this system are presented for metal and rock samples, as well as samples with artificial anomalies.

Most recently Datta [1995] had developed a methodology in ultrasonic NDE for identification and reconstruction of defects in fibre composites. He used Algebraic Reconstruction Technique (ART) for reconstruction.

## 1.9 Thesis Layout

\* Chapter 2 gives the detail of the data collection and the algorithm used for reconstruction.

\* Chapter 3 gives the detail of the experimental ultrasonic set-up used for scanning the specimen using ultrasonic CT scanner.

\* Chapter 4 describes the details of the program used for reconstruction, simulation and color coding. It also gives the reconstructed images for simulated data for validation of CBP and discussions on the results of the simulated images obtained from the simulated data.

\* Chapter 5 provides discussions on the results based on the real data.

\* Chapter 6 summarizes the conclusion and suggest scope for the further works.

## Chapter 2

# Theoretical Formulation

In this Chapter, the CT related computational and mathematical procedures underlying the data collection, image reconstruction, display are discussed.

### 2.1 Preliminaries

$$\int_c \mu(r, \phi) dl = p(s, \theta) \quad (2.1)$$

where  $p(s, \theta)$  is called the projection data for the tomographic algorithm, and it is the line integral of function along the line specified by  $s$  and  $\theta$ . (see Fig 2.1)

Now the aim is to recover the value of  $\mu(r, \phi)$ , the slowness coefficient, if a set of several  $p$ -values measured along various chords is given. This is the fundamental problem of CT and CBP has been used in the present study for that purpose. The  $\mu$  values can be suitably normalised to get the density values, if so desired.

## 2.2 Data Collection Mode

The image processing methodology requires the slowness data to be collected by an array of ultrasonic receivers for the reconstruction of the function  $\mu(\tau, \phi)$ .

In this study the mode of collection is parallel-beam (PBG) mode (Fig.2.1). This system consists of several pairs of ultrasonic transmitters (S) and ultrasonic receivers (D) which can scan the object completely.

The S-D pairs are spaced uniformly and the object can be rotated to get the data for different views. The line SD represents the path of the data ray or the chord along which 'p' values is found out.

The perpendicular distance from the center of the object to the path of the ray is denoted by  $s$ . Several SD pairs could be used to get the  $p$  data. The object table is rotated to get the several sets of  $P$  for different values of  $\theta$ .

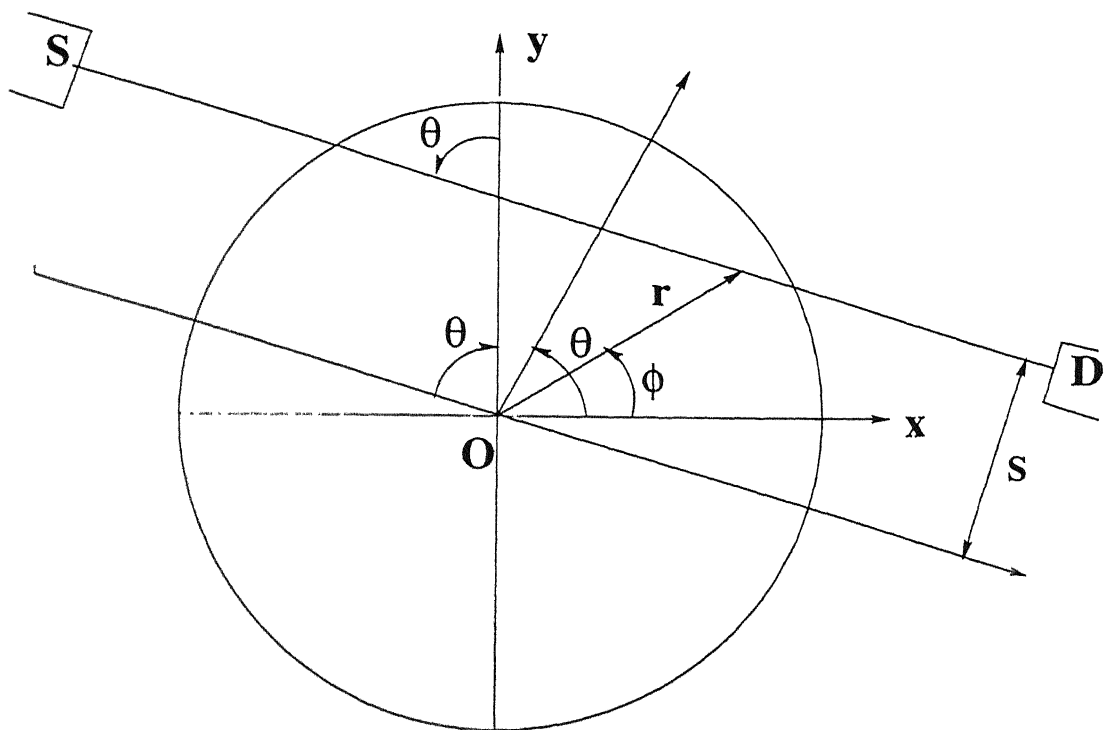
## 2.3 The CBP Algorithm

The convolution back projection (CBP) algorithm has been described in detail by Herman (1980), In this section we review CBP briefly as reported earlier by Munshi (1992).

Fig. 2.1 shows the data collection geometry for a parallel beam ultrasonic scanner. The object function  $f(r, \phi)$ , is represented by a unit circle and on (of many) data rays is represented by SD. The ray indices are  $s$  and  $\theta$ , where  $s$  is the perpendicular distance of the ray from the object center, and  $\theta$  is the angle of source position (or object rotation). The CT data is denoted by  $p(s, \theta)$  given by

$$p(s, \theta) = \int_{SD} f(r, \phi) dz \quad (2.2)$$

Here,  $z$  is the variable of integration along the chord SD. The ultrasonic setup collects



S-Source  
D-Detector

Figure 2.1: Parallel Beam Data Collection Geometry

the projection data  $p(s, \theta)$  for many values of  $s$  and  $\theta$ .

The “Projection- Slice” theorem [Herman (1980)] states the equivalence of the two-dimensional Fourier transform of  $f(r, \phi)$  and the 1-dimensional Fourier transform of  $p(s, \theta)$  with respect to  $s$ . Symbolically

$$\hat{p}(R, \theta) = \hat{f}(R \cos \theta, R \sin \theta) \quad (2.3)$$

Where the symbol  $\wedge$  represents the Fourier transform and  $R$  is the Fourier frequency.

A two-dimensional Fourier inversion of Eq.(2.4) leads to the well known tomographic inversion formula,

$$f(r, \phi) = \int_0^\pi \int_{-\infty}^{+\infty} \hat{p}(R, \theta) e^{i2\pi R r \cos(\theta - \phi)} |R| dR d\theta \quad (2.4)$$

Where,

$$\hat{p}(R, \theta) = \int p(s, \theta) e^{-i2\pi R s} ds. \quad (2.5)$$

We note that the inner integral in Eq.(2.5) is divergent. A practical implementation of Eq.(2.5) incorporates the replacement of the factor  $|R|$  by  $|R| W(R)$ , where  $W(R)$  is a suitable window function which vanishes outside the interval  $[-R_c, R_c]$ . Here  $|R_c|$  is the Fourier cut-off frequency. Normally  $W(R)$  is an even function of  $R$ . Thus Eq.(2.5) takes the approximate form,

$$\tilde{f}(r, \phi) \approx \int_0^\pi \int_{-\infty}^{+\infty} \hat{p}(R, \theta) e^{i2\pi R r \cos(\theta - \phi)} |R| W(R) dR d\theta \quad (2.6)$$

If  $\hat{p}(R, \theta)$  also vanishes for  $|R| > R_c$ , then the reconstructed  $\tilde{f}$ , denoted by  $\tilde{f}$ , agrees exactly with  $f$  the following window,

$$W(R) = \begin{cases} 1, & |R| \leq R_c \\ 0, & |R| > R_c \end{cases} \quad (2.7)$$

An implementation of Eq.(2.7) in the spatial domain exploits the convolution theorem of Fourier transform so that the reconstruction,  $f$ , is given by,

$$\bar{f}(r, \phi) \approx \int_0^\pi \int_{-\infty}^{+\infty} p(s, \theta) q(s' - s) ds d\theta \quad (2.8)$$

Where,

$$q(s) = \int_{-\infty}^{+\infty} |R| W(R) e^{i2\pi R s} dR \quad (2.9)$$

and,

$$s' = r \cos(\theta - \phi) \quad (2.10)$$

The index  $s'$  is of the data ray passing through  $(r, \phi)$ , the point being reconstructed. The inner integral in Eq.(2.8) is a 1-dimensional convolution, and the outer integral (corresponding to the averaging operation over  $\theta$ ) is termed as back projection, and hence, the name convolution back projection for this particular implementation. The CBP method is also known as the filtered backprojection algorithm due to the 'filtering' of the Fourier transform of the projection data,  $\hat{p}$ , by the window ( or filter)  $W(R)$  in the initial stages of formulation as given by Eq. (2.6). The function  $q(s)$  known as the convolving function, is evaluated once and stored for repeated use for different views ( or different angle  $\theta$  ). So, for a given point  $(r, \phi)$ , the inherent error  $E_1$ , in the CBP implementation, Eq.(2.8) is,

$$E_1(r, \phi) = f(r, \phi) - \bar{f}(r, \phi) \quad (2.11)$$

Where  $f$  and  $\bar{f}$  are given by Eq.(2.4) and Eq.(2.6) respectively. This error is strictly due to infinite cut-off,  $R_c$ , of the Fourier frequency and is precisely zero if the projection data happens to be band-limited and the cut-off frequency is chosen to be the highest frequency contained in  $\bar{p}$ . In general, to avoid aliasing artifacts [Herman(1980)], it is recommended to choose,

$$R_c = 1/(2\Delta s)$$

Where  $\Delta s$  is the spacing of the data rays.

It has been shown [Munshi(1992)] that  $E_1$  at a given point  $(r, \phi)$  in the object cross-section, is given by

$$E_1(r, \phi) \approx k(W'''(0))(\nabla^2 f(r, \phi)) \quad (2.12)$$

Where,

$$W'''(0) = \left. \frac{\partial^2 W(R)}{\partial R^2} \right|_{R=0} \quad (2.13)$$

$\nabla^2 f$  is the Laplacian of  $f$ ,

and,  $k$  is a constant depending on the data-ray spacing. Eq.(2.12) is valid for objects having certain smoothness properties provided the data is perfect as per Eq.(2.2).

The error  $E_1$  represents the point-wise theoretical error in reconstruction, and it also obvious that the Laplacian of  $f(r, \phi)$  has to exist for the predictions of the theorem to be valid. For points in the cross section, where  $\nabla^2 f$  does not exist, the linearity between  $E_1$  and  $W'''(0)$  is disturbed. If  $\nabla^2 f$  is zero, other errors will be more dominant. The Laplacian

is zero for smooth regions of the objects, while it does not exist for rough edges. For simulated objects,  $E_1$  can be calculated from the original image, but for real objects the distribution is unknown, hence the error in reconstruction cannot be calculated directly. This fact motivates an indirect representation of error. It has been reported earlier (Munshi et al [1997], Davis et al [1996]) that, for a given data set, sharpness can be used as an indicator of the behaviour of error, arising due to the choice of the filter function.

If the image consists of a single point then the sharpness parameter is defined as the values of the reconstructed grey level at that point. For a general image, the sharpness parameter corresponds to,  $NMAX$ , the maximum grey level (linear slowness coefficient) in the reconstruction.

In the present work  $1/NMAX$  (inverse of sharpness) along with Eq.(2.12) has been used to represent the physical nature of the object cross section.

## Chapter 3

# Experimental Set-up and Procedure

### 3.1 Present Set-up

This Chapter describes the details of the experimental set-up, used for this study, to perform automated ultrasonic tomography. This involves generation of the ultrasonic pulse, conversion of recieved signal into digitized form in the real time and the storing of the data. This set-up gives the Tomographic images of the specimens.

The present automated ultrasonic system, consist of a scanning tank, a high resolution type Ultrasonic Flaw Detector (UFD), transducer, a high speed analog to digital converter (A-D) board and other accessories for precision movement of the transducers in two dimensions and data collection. The software controls the precision movements of the probes using stepper motors, digitize the recieved waveform and store it on the hard disk of the computer. The A-D board and PC-AT 386 machine, can digitize the ultrasonic signal in real time. A brief description about the set-up and the experimental procedure

for automated probe movement and data acquisition is outlined in the following sections.

## **3.2 Components of Experimental Set-up**

### **(1) Scanning Tank**

The purpose of the scanning tank is to house the stepper motors, the probes and the composite specimen. As is the common practice, the probes and the specimens are submerged in water which acts as a coupling medium. The side walls of the coupling tank are made of transparent perspex. Two lead screws, each having a pitch of 4mm, are fixed in mutually perpendicular directions on a frame located at the top of the tank. Each lead screw, mounted on frictionless ball bearings, is independently run by a separate stepper motor. The probe holder is mounted on a mechanical base acting as a nut of the lead screw. The schematic diagram and a photographic view of the set-up are shown in the Fig. 3.1 and Fig. 3.2 respectively. The probes can be moved very accurately as the lead screws are of zero backlash grade.

### **(2) Ultrasonic Flaw Detector**

For generating ultrasonic waves and collecting the recieved signal an ultrasonic flaw detector (Krautkramer-Branson make, USIP 12) is used. The generated wave by the UFD can either be used in narrow band region or broad band region depending on the type of application. The UFD can be used with a single probe for pulse echo method or with two probes for through-transmission method. The recieved signal can be obtained from the UFD in rectified or in radio frequency (RF) mode. The gain of the recieved signal can be adjusted by fine controls to the desired level to reduce noise and avoid any saturation. The time base can be adjusted to clearly examine the successive echoes. Apart from these,

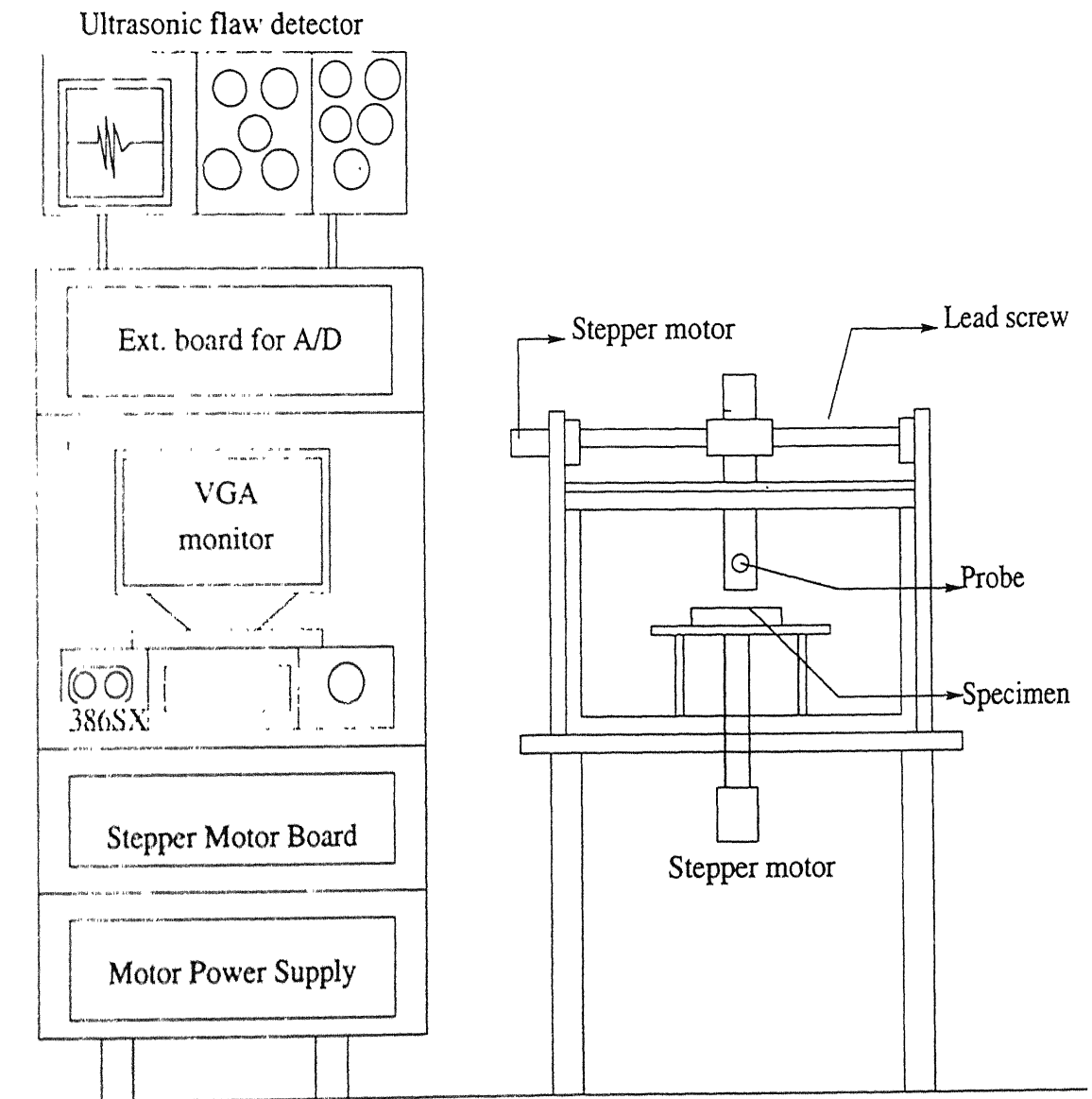


Figure 3.1: Schamatic Diagram of Ultrasonic Setup

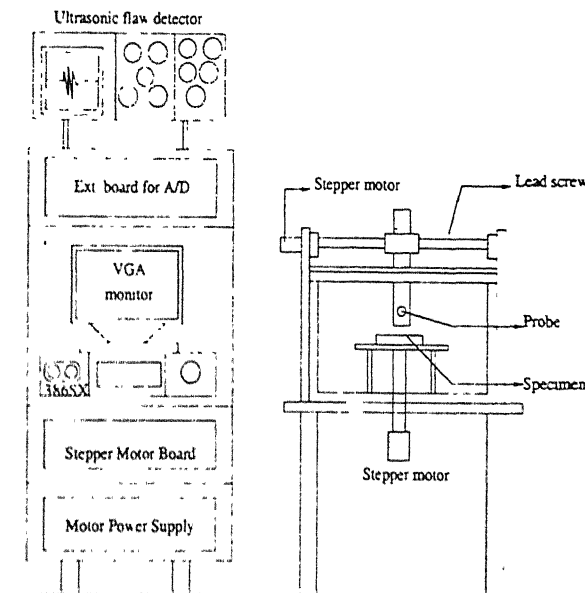


Figure 3.2: Photographic view of the Ultrasonic Setup

the UFD is also furnished with facilities such as noise reject, selection of two simultaneous time gates with threshold values, alarm facility and distance amplitude correction (DAC). The probes are connected to the UFD through standard LEMO connectors and the RF signal can be tapped from the UFD through a standard BNC socket for digitization.

### (3) Computer

The set-up is run through a microcomputer of PC-AT 386 SX family which is interfaced with the hardware i.e., stepper motor driver board and ultrasonic flaw detector via A-D converter. The scanning procedure is completely controlled by the computer when the scanning code is executed. The computer, with the storage capacity of 300 MB, is also networked with the central super mini computers so that the collected data can be directly sent to the systems for post processing.

## **(4) Stepper Motors**

The stepper motors used in the present set-up are of type STM 601 with 12v input. The torque capacity of the motor is 2 kg-cm. The maximum step rate is 1023. The motors can be moved either in clockwise or counterclockwise. The motors are operated by the pulses sent from the driver board, the number of clock pulses for one revolution being 200. For one revolution of the screw the probes move by 4 mm.

## **(5) Stepper Motor Controller**

The PCL-211 stepper motor control card, (manufactured by Dynalog Micro Systems), is used to drive the stepper motors in precise increments, direction, and speeds. Very accurate repeatable movements of the motor can be achieved. With this card a maximum of three motors can be controlled simultaneously. Each independent stepper channel consists of a 8039 processor that can execute a set of motion control commands. Every 8039 processor also comes with an on board ROM where the control program for the processor resides. All commands set by the PC are executed by the processor running the relevant control program. Once the command is set, the PC is set free, thus optimum utilisation of PC resources being possible.

## **(6) Analog to Digital Converter**

The recieved RF signals from the UFD is digitized using a Matec A-D board. The board is capable of digitizing the RF signals with a maximum sampling rate of 100 MHz and maximum data acquisition flexibility through a 64k on-board high speed memory buffer. The various board functions, under software control, are input channel selection, AC/DC coupling, input voltage range, RF/Video mode, sampling rates, trigger selection, clock

control, threshold phase and level, board selection and interrupt e. 5  
high speed data acquisition memory is mapped directly into PC memory.  
wave form has been captured, the PC can transfer data off the board at  
bit) or 3 MHz rate (16 bit) using simple memory block instructions. This b  
freedom from the static architecture of a stand alone instrument and the con.  
D100A oscilloscope is used to examine the waveform for selecting the appropriate  
parameters such as delay, gate start, gate length etc.

## (7) Transducers

The transducers (probes) used in the present investigation is E16B which generates broad band longitudinal waves. The diameter of the transducer is 10mm. They are connected to the UFD by water proof connectors. The fixtures hold the transducer in vertical position.

## 3.3 Specimen Preparation

The present investigations were performed on composite with polystyrene as the reinforced material and perspex as the matrix material. The specimen are of circular shapes with diameter 60 mm and following are the description of the specimen used.

### SPECIMEN 1 (E1):

A 40 mm circular inclusion at the geometric center is made. First 40 mm hole is made in the perspex and the paste of polystyrene is filled inside the hole. The specimen is heated inside the oven to harden the resin. This specimen is as shown in Fig. 3.3.

### SPECIMEN 2 (E2):

In this specimen a 15 mm circular inclusion is made. The procedure of making this specimen is same as for the previous specimen. This specimen is as shown in the Fig. 3.4.

#### SPECIMEN 3 (E3):

In this specimen a 25 mm x 25 mm square inclusion is made at the geometric center. The procedure for preparing the specimen is same as for the specimen1. The above specimen is as shown in the Fig. 3.5.

#### SPECIMEN 4 (E4):

4) This specimen is made up of two circular inclusion of different sizes. One inclusion is of 15 mm diameter and other inclusion is of 10 mm diameter and both these inclusions are at the diameter of the specimen. The spacing between these two is 20 mm. The procedure for preparation is same as that of specimen1. This specimen is as shown in the Fig. 3.6.

These circular specimen are housed inside a square wedge as shown in Fig. 3.7. with a circular hole of 60 mm diameter. This is done to ensure the normal incidence of the ultrasonic wave so that the transmission through the specimens is maximum and the data for as many views can be collected. Earlier when square wedges are used, projections were limited because for each projection a separate set of wedges were required. So this problem is over come by choosing circular specimens and a wedge as shown in Fig. 3.7.

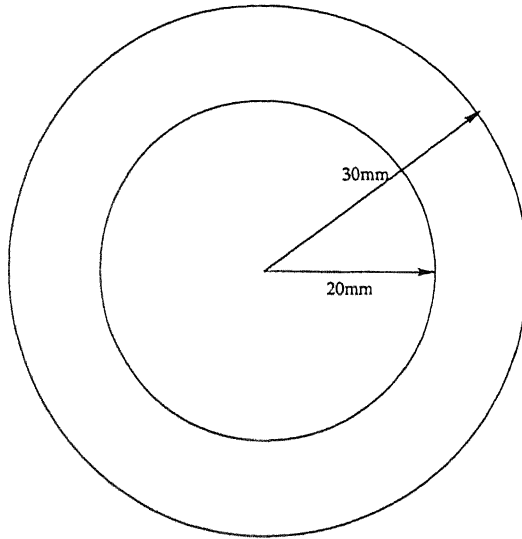


Figure 3.3: Specimen 1

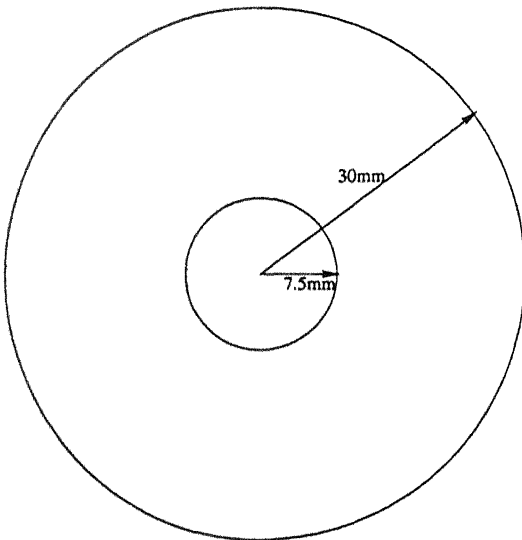


Figure 3.4: Specimen 2

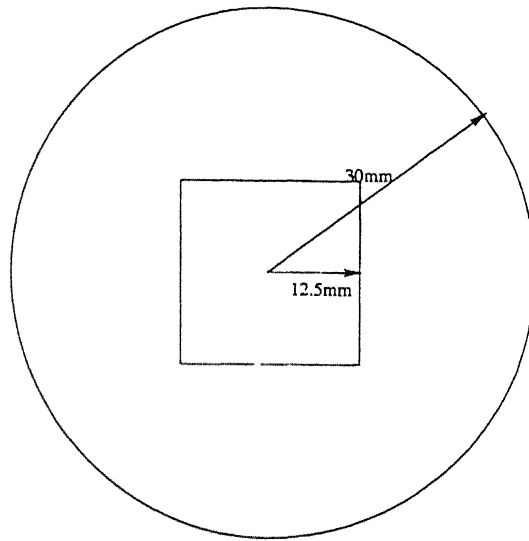


Figure 3.5: Specimen 3

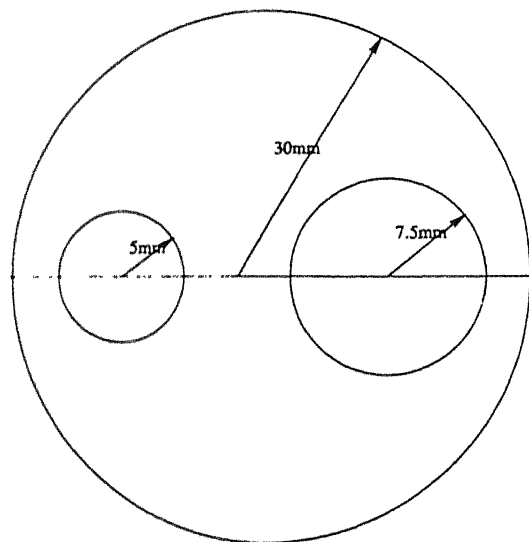


Figure 3.6: Specimen 4

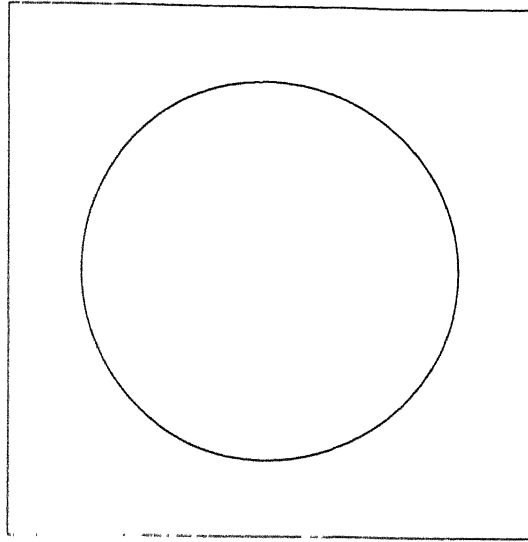


Figure 3.7: Wedge

### 3.4 Experimental Procedure

The specimen to be investigated is cleaned and put on the rotatory table inside the square wedge. The probe is brought by moving the motor to the starting position as shown in the Fig. 3.1. It is ensured that the probe and the specimen are completely immersed in water. The distance between the probe surface and the specimen is so adjusted that they are at minimum distance without touching each other. The gain adjustment controls are so adjusted that the peak of the signal does not exceed 80% of the maximum screen height of the UFD to avoid saturation. The RF signals from the UFD can be viewed on the digital oscilloscope provided by the software of the A-D board. The gate parameters on the signal to be digitized are chosen and corresponding changes are made in the data file. Once the initial settings are done scanning of the specimen can be started by executing the master scanning code. The data collected is stored in the files on the hard disk in append mode. The scanning can be interrupted at any intermediate stage and

restarting can be done from the point where it was interrupted. The peak amplitude of the signal in the frequency domain are extracted during the scanning process. To reduce the time dependent error, peak amplitude detection at any location is repeated over a number of times and the average value is taken.

## Chapter 4

# Data Analysis

### 4.1 Numerical Implementation of the Programme for Discrete Data

In practical application of reconstructions, the measured data correspond to the estimates of  $p(s, \theta)$  for numerous values of  $s$  and  $\theta$ . And the aim is to find the function  $\mu(r, \phi)$ .

Further, for the simplification of the reconstruction algorithm the projections are sampled uniformly in both  $s$  and  $\theta$ . Therefore, for each view there are  $M$  equi-spaced rays  $\Delta s$  apart, and  $N$  such views  $\Delta\theta$  apart. We define

$$\left. \begin{aligned} M^+ &= (M - 1)/2 \\ M^- &= -(M - 1)/2 \end{aligned} \right\} \text{For odd } M$$

$$\left. \begin{aligned} M^+ &= (M/2) \\ M^- &= -(M/2) \end{aligned} \right\} \text{For even } M$$

In order to ensure that the collection of rays specified by

$$\{(m\Delta S, n\Delta\theta) : M^- \leq m \leq M^+, 1 \leq n \leq N\}$$

covers the unit circle from a complete range of directions, we choose

$$\Delta\theta = \pi/N$$

and  $\Delta s = 1/M^+$

## 4.2 Programme for Simulating Data

The simulated data has been generated by Kumar [1996] for the following cases:

1. Unit circle (S1).
2. Unit circle with a hole of 0.3 unit radius (S2).
3. Annular hole in the unit circle (S3).
4. Rectangular cross-section with nine holes of different sizes at different locations (S4).

The number of rays,  $N_{RAY}$  and the number of views,  $N_{ANGLE}$  can be varied as per the need. The programme written is a general one. For circular geometries, the region has been divided into three sectors of radius  $r_1, r_2, r_3$  and the absorption coefficient  $f_1, f_2, f_3$  respectively. For rectangular geometry also the programme will work for any number of holes.

## 4.3 Programme for Reconstruction

The convolution backprojection algorithm uses the data of parallel beam geometry to reconstruct the image of a cross-section.

The projection data has been kept in the input file after applying the correction due to wedges which are used so that the incident ray must be normal to the test specimen. If the incidence is not normal, large part will be reflected then the transmitted, so a very weak signal at the ultrasonic receiver. The programme writes the reconstructed CT numbers in the result file which besides CT numbers also contain maximum, minimum, cross sectionally averaged and the centerline averaged LITF values. In the present work eight filters have been used to study the tomographic image. Beside the Ramachandran-Lakshminarayan filter, sine, cosine and five Hamming filters have been used for different values of  $B$ , i.e.  $B = 0.54, 0.75, 0.80, 0.91$  and  $0.99$ . Where Hamming filter with  $B = 0.54$  is called Hamming smooth filter and Hamming filter with  $B = 0.99$  is called Hamming sharp filter. The following filters are given by :

$$W(R) = \begin{cases} 1 & \text{Ram - Lak} \\ \frac{\sin(\pi R/2R_c)}{\pi R/2R_c} & \text{Sin} \\ \cos(\pi R/2R_c) & \text{Cos} \\ B + (1 - B)\cos(\pi R/R_c) & \text{Hamming} \\ & (0.5 \leq B < 1.0) \end{cases}$$

The details of the filters are listed in Table 4.1 with their Fourier-Space origin second derivatives,  $|W''(0)|$ .

Filter code	$B$	$W_H(0)$
Ram-Lak	-	0.000
Sin	-	0.083
Cos	-	0.250
h99	0.999	0.001
h91	0.917	0.083
h80	0.800	0.200
h75	0.750	0.250
h54	0.540	0.460

Table 4.1: Filter details

## 4.4 Programme for Displaying Reconstructed Image and Colour Levels

For the purpose of displaying the image, the CT numbers from the result file is read and the appropriate colour is assigned corresponding to that. At the position of each number a small rectangle is drawn and filled with gray level corresponding to that CT number. The image produce is a pixel. Thus by generating pixels for each CT numbers at their positions they can be graphically displayed. The colour code is printed adjacent to it for quick reference

## 4.5 Colour Code

The colour code is must to understand and extract information from the colour images produced in the present work. The natural choice for the colour code was our own solar spectrum "VIBGYOR" in the scale 0 to 255. Number 0 is represented by 'Voilet' ann 255 by 'Red' and the intermediate colours are linearly interpolated to represent other numbers.

Reconstruction of tomographic data results in a matrix in which each element corresponds to the magnitude, of the material property being observed, at that point. If we

are able to view this matrix in the form of a coloured image, each colour in the image will correspond to the different observed values of the material property, thus providing us with a view to the inside object under observation. The VIBGYOR pattern provides a good mode of visualizing this variation in the material properties of the object. This visualization had been extremely simple if we had a fixed number of values for the observable material property and we had a unique identifier for each colour in a VIBGYOR spectrum. Thus the problem can be broken up into two parts:

- 1 Identifying the RGB values for each of the colours required along the VIBGYOR spectrum.

- 2 Assigning the elements of the matrix to one of these colours based on a linear scaling of all the values in the matrix.

It is a common practice to represent a colour as a set of three numbers, which correspond to the intensities of Red, Green and Blue respectively, that when mixed would produce the colour. To tackle the first problem, we took the RGB values of the seven main colours of the rainbow as:

- Violet: 148, 0, 211
- Indigo: 75, 0, 130
- Blue : 0, 0, 255
- Green : 0, 255, 0
- Yellow: 255, 255, 0
- Orange: 255, 165, 0
- Red : 255, 0, 0

In each case 0 corresponds to the minimum possible intensity and 255 corresponds to the

maximum possible intensity of the colour (Red, Green or Blue). The program prompts the user to enter the number of colours desired along the VIBGYOR spectrum. Keeping the values of the major colours as given above, the other values are computed by linearly interpolating the Red, Green and Blue colour components between these major colours. If 50 colours are required to lie between Blue and Green, then the Red component of all these colours is assigned a value of zero and the Green component is calculated as  $Green_i = 0 + ((255 - 0) * i/50)$ , and similarly the Blue component of these colours is calculated as  $Blue_i = 255 + ((0 - 255) * i/50)$ .

The second sub problem is also tackled by using linear interpolation. The minimum and maximum values occuring in the matrix are determined first. If the number of colours required by user is  $n$ , then  $n - 2$  values lying evenly spaced between the two limiting values are computed. Now we have  $n$  values corresponding to each of the  $n$  required colours. While displaying the image the colour to be assigned to each pixel is determined by comparison with these  $n$  values. This can be better understood in light of the following example. Suppose the user asks for a 256 colour long VIBGYOR spectrum, let the smallest value found in the matrix is  $V_{min}$  and the largest value is  $V_{max}$ . An array of 256 numbers is created and  $V_{min}$  and  $V_{max}$  are placed in the first and the last place, respectively. These and the other 254 values can be computed using the formula:

$$V_i = V_{min} + (V_{max} - V_{min}) * i/255 \quad 0 < i < 255$$

## 4.6 Validation of CBP from Simulated Data

The simulated data of Kumar [1996] have been studied for four different samples as mentioned in the section (4.2). The results have been summarised in table 4.2 to table 4.5. The original and the reconstructed images are shown in Fig. 4.3 to Fig. 4.10. Re-

construction has been done for h54 and h99 filters. Unit circle is easiest to reconstruct and gives the most accurate reconstruction. These samples has been chosen to represent the flaws in the test specimens with increasing complexity.

By looking at the reconstructed images, we conclude that the results obtained are good. The quality of reconstruction of simulated objects are very good because of absence of any error but the error in CBP algorithm. The gray level is symmetrical for symmetrical objects.

The gray-level do not changes sharply at the edges as in the actual objects. Thus the edge effects are visible. But the density of the reconstructed section of simulated data is uniform at 4 to 6 pixel away from the edge of the pixel boundary.

The above analysis on the simulated objects shows that CBP algorithm can give good results for the symmetric as well as for non-symmetric objects.

Fig. 4.1 and Fig. 4.2 shows the comparative performance ( $1/NMAX$ ) of filters for simulated samples. Referring to section 2.3, for a given cross-section distribution  $f(r, \phi)$ , the pointwise error in reconstruction is proportional to the magnitude of  $W''(0)$ , provided that the collected data are "perfect", and the specimen characteristics around the point in question is such that Eq.(2.12) is valid [Davis et al. (1995)]. So processing of a given data set by several filters results in a linear relationship between  $W''(0)$  and  $E_1$ . The plots have been shown in from Figs. 4.1 and Fig. 4.2. The plot for simulated specimens S1, S2 and S3 shows wide variation from linearity. Since these samples are smooth,  $\nabla^2 f$  vanishes for the major portion of the region, hence, Eq.(2.12) no longer represents total error in this case. Fig. 4.2 show good linear fit because for this sample  $\nabla^2 f$  exist

Filters	NMIN	NMAX	1/NMAX
h54	25	75	0.013333
h75	25	76	0.013157
h80	25	78	0.012987
h91	25	81	0.012345
h99	25	82	0.012048

Table 4.2: Summary of results for simulated specimen 1

Filters	NMIN	NMAX	1/NMAX
h54	22	75	0.013333
h75	23	76	0.013157
h80	22	78	0.012827
h91	18	81	0.012345
h99	16	83	0.012048

Table 4.3: Summary of results for simulated specimen 2

Filters	NMIN	NMAX	1/NMAX
h54	24	77	0.01298
h75	24	76	0.01315
h80	24	78	0.01282
h91	23	82	0.01219
h99	21	84	0.01190

Table 4.4: Summary of results for simulated specimen 3

Filters	NMIN	NMAX	1/NMAX
h54	22	54	0.01851
h75	21	55	0.01818
h80	21	56	0.01785
h91	20	56	0.01785
h99	19	57	0.01754

Table 4.5: Summary of results for simulated specimen 4

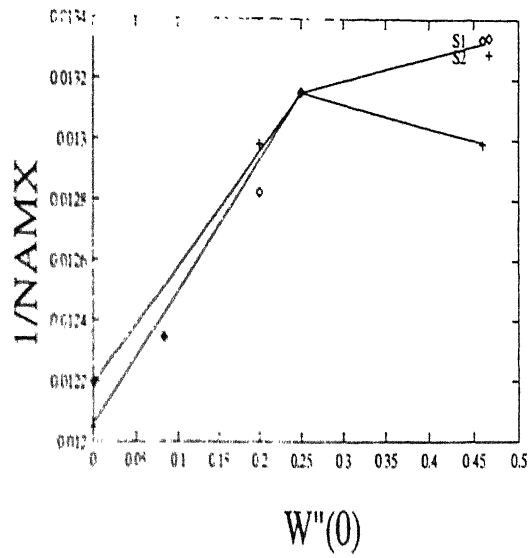


Figure 4.1:  $1/NMAX$  plot for simulated specimens

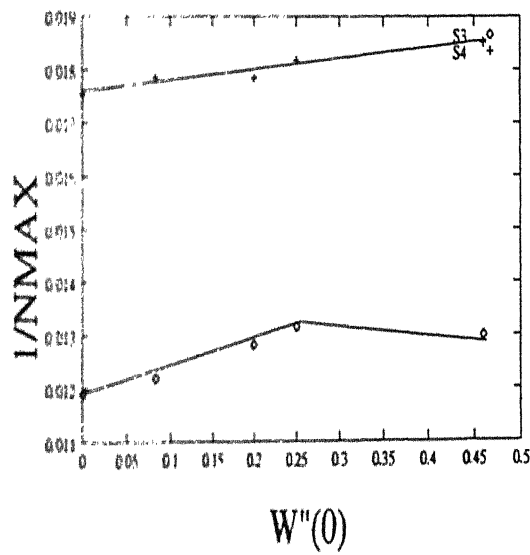


Figure 4.2:  $1/NMAX$  plot for simulated specimens

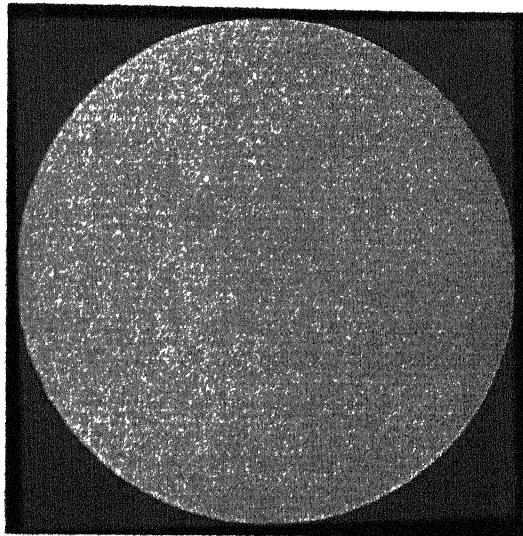
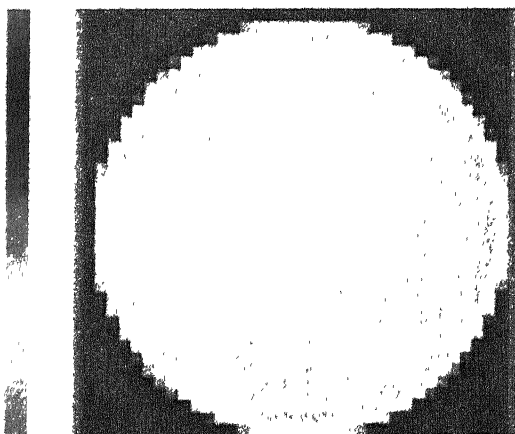
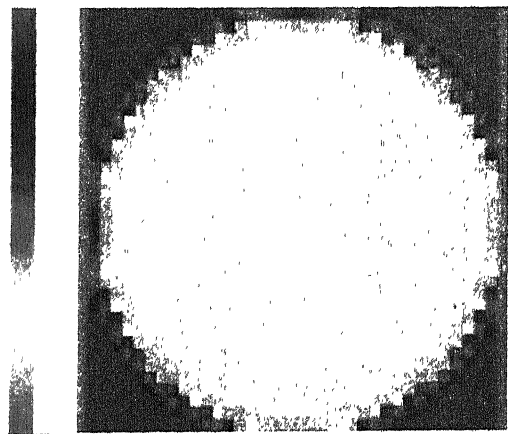


Fig. 4.1 : Original Image for the simulated specimen 1



Min = 1.0000      Max = 229.0000  
 LAvg = 0.9707      AAvg = 0.8241  
 File : h54.fl, NRay : 37, NView : 60



Min = 1.0000      Max = 256.0000  
 LAvg = 0.9727      AAvg = 0.8068  
 File : h99.fl, NRay : 37, NView : 60

Fig. 4.2 : Reconstructed image with h54 and h99 filters

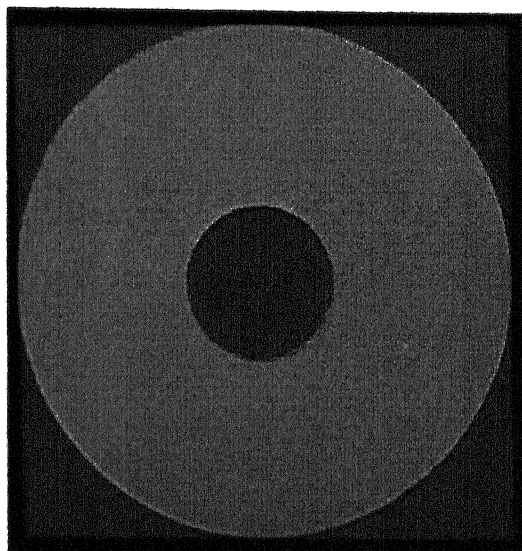
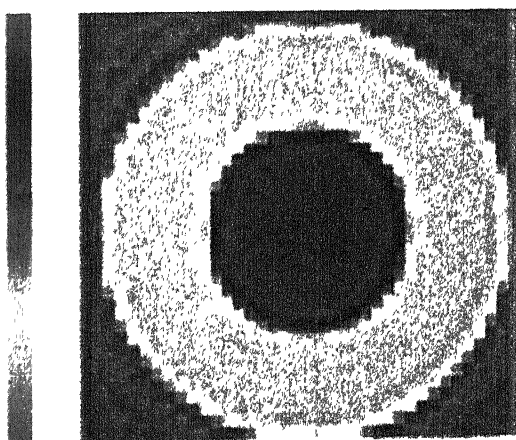
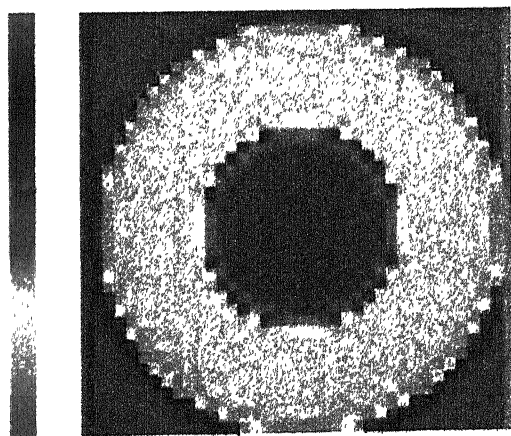


Fig. 4.3: Original Image for the Simulated Specimen 2



Min = 23.0000      Max = 233.0000  
 LAvg = 0.4856      AAvg = 0.6338  
 File : h54.fl, NRay : 37, NView : 60



Min = 1.0000      Max = 256.0000  
 LAvg = 0.4855      AAvg = 0.6111  
 File : h99.fl, NRay : 37, NView : 60

Fig. 4.4: Reconstructed Image with h54 and h99 filters

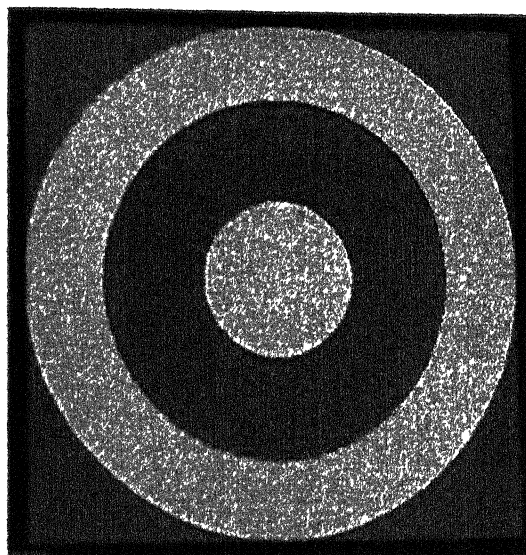
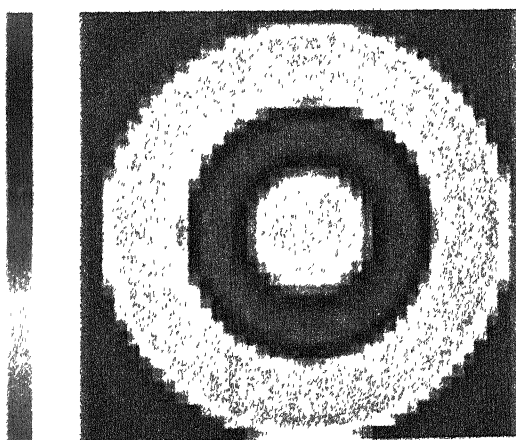
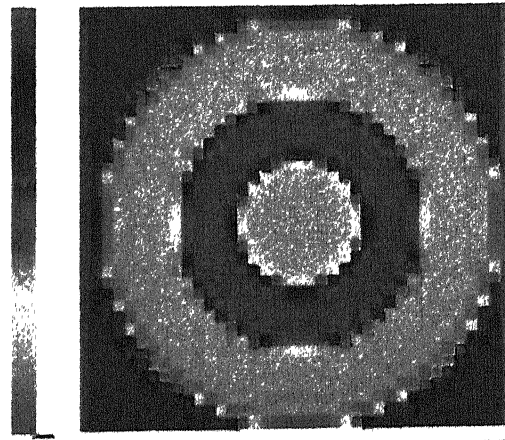


Fig. 4.5: Original Image for the Simulated Specimen 3



Min = 13.0000      Max = 227.0000  
 LAvg = 0.6763      AAvg = 0.6185  
 File : h54.fl, NRay : 37, NVlew : 60



Min = 1.0000      Max = 256.  
 LAvg = 0.6776      AAvg = 0.5  
 File : h99.fl, NRay : 37, NVlew : 60

Fig. 4.6: Reconstructed Image with h54 and h99 filters

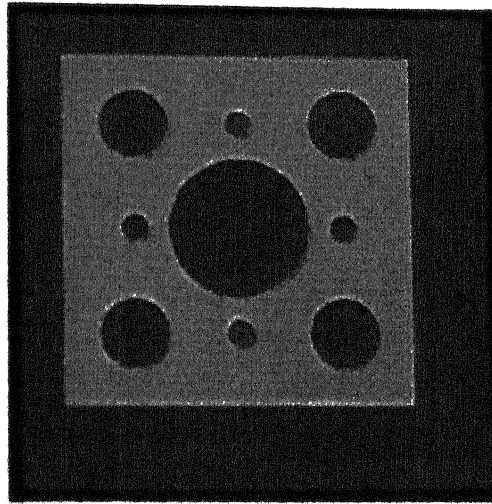
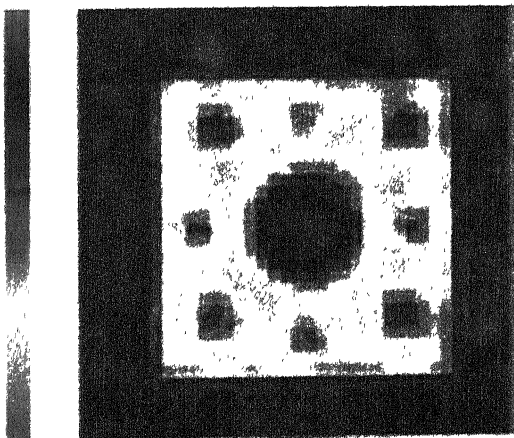
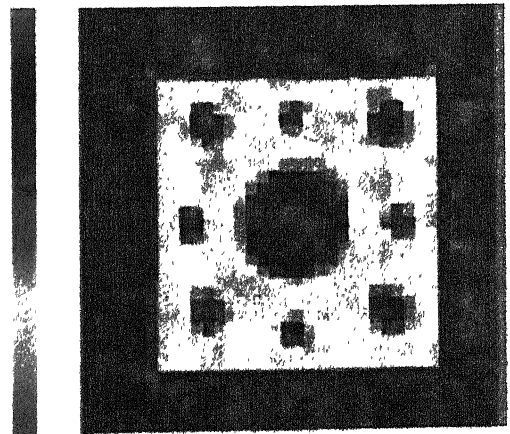


Fig. 4.7: Original Image for the Simulated Specimen 4



Min = 21.0000      Max = 235.0000  
 LAvg = 0.1604      AAvg = 0.1907  
 File : h54.tif, NRay : 37, NView : 60



Min = 1.0000      Max = 256.0000  
 LAvg = 0.1425      AAvg = 0.1902  
 File : h99.tif, NRay : 37, NView : 60

Fig. 4.8: Reconstructed Image with h54 and h99 filters

## Chapter 5

# Experimental results and Discussion

In this Chapter, the results obtained from the actual experimental data have been discussed.

### 5.1 Data Used

The data used was taken with the help of an ultrasonic setup. The details are briefly summarized here.

a) The ultrasonic transmitters and receivers are fixed horizontally at a distance of 9.35 cm. The ultrasonic probe which is used is of 5 MHz frequency. This set of transmitter and receiver are moved in a horizontal direction at a regular step of 1 mm upto 90 mm.

b) The specimen was fixed on the rotating table which can be rotated with the help of a stepper motor or manually. Here manual rotation was used. The specimens are rotated by 90 degrees upto 180 degrees to scan the specimen completely.

c) The data is collected for four different specimen in which two are radially symmetric, one is quadrant symmetric and the last specimen is unsymmetric. All the specimen are made of perspex and the inclusion material is polystyrene. The acoustic impedance of these two material is differ by 10% .The information of the different specimen is as follows:

**(i) SPECIMEN 1 (E1)**

This specimen is a circle with radius 30 mm and a circular inclusion at the center of radius 20 mm. The geometry of this specimen is shown in Fig. 5.3. This specimen is scanned with 90 rays and for 90 views. The distance between two consecutive rays is 1 mm.

**(ii) SPECIMEN 2 (E2)**

This specimen is also a circle as the previous specimen but here the circular inclusion is of radius 7.5 mm. The geometry of this specimen is shown in Fig. 5.5. Here also the specimen is scanned with 90 rays and for 90 views. Here also the distance between two consecutive rays is 1 mm.

**(iii) SPECIMEN 3 (E3)**

This specimen is circle with radius 30 mm and a square inclusion at the center of length 25x25 mm. The geometry of this specimen is shown in Fig. 5.7. This specimen is scanned with 90 rays and 20 views. Here also the distance between the two consecutive rays is same as the previous specimen.

**(iv) SPECIMEN 4 (E4)**

This specimen is also a circle with radius 30 mm and two circular inclusion at the diameter of 15 mm diameter and 20 mm diameter respectively and the distance between them is 25 mm. The geometry of this specimen is shown in Fig. 5.9. This specimen is

also scanned with 90 rays and 20 views.

## 5.2 Discussion of the Results

The results of the experiments done on four different specimens with eight different class of filters are obtained. But we take only two filters Hamming 54 (h54) and Hamming 99 (h99) for discussion. As all the results with different filters are more or less similar to these results or lies between these two. Discussion on the results of the experiments is as follows

### (i) SPECIMEN 1 (E1):

The original and the reconstructed image of the specimen are as shown in the Fig. 5.3 and Fig 5.4. The first part of the Fig.5.4 is reconstructed with Hamming smooth filter i.e h54 and the second part is reconstructed with Hamming sharp filter i.e. h99. In both the reconstructed images the inclusion is clearly seen at the center of the specimen but which is of small size as compared to the inclusion in the original image. The reason for this is as the ultrasonic ray traverse a medium whose acoustic impedance is different from the one in which it is travelling, it bends around the inclusion due to which time of flight increases and reduces the size of the inclusion. There are two circle visible of different radii which is due to the following two reasons.

- (a) Wobble in the rotating table of the ultrasonic setup and
- (b) The mismatch in the centres of the specimen, specimen holder and the rotating table

There is some error also because of the water in between the specimen and the wedge.

### (ii) SPECIMEN 2 (E2):

The original and the reconstructed image of this specimen are as shown in Fig. 5.5

and Fig. 5.6. This specimen is also reconstructed with two different filters h54 and h99. Here the inclusion of smaller radii as compared to the previous specimen is very clearly seen. Same explanation above is also valid for this specimen also.

**(iii) SPECIMEN 3 (E4):**

The original and the reconstructed image of this are shown in Fig. 5.7 and Fig. 5.8. This specimen is also reconstructed with two different filters h54 and h99. Here some lines in the star formation are clearly visible which are due to the lesser views in scanning the specimen. The inclusion at the center is not a square which is due to the sharp edges at the square corners and due to which ray bending effect is more. So from the reconstructed image defect can be detected but with some truncated edges.

**(iv) SPECIMEN 4 (E4):**

The original and the reconstructed image of this specimen is shown in the Fig. 5.9 and Fig. 5.10. This specimen is also reconstructed with two different filters Hamming 54 and Hamming 99. With Hamming sharp (h99) filter high frequency components are clearly visible which are not in the Hamming smooth (h54) filter. Here many small inclusions in place of two bigger inclusions are visible. The exact size of the inclusion is not determined because when ultrasonic wave traverses two inclusions the path it travel is not straight and because of which error are introduced in the reconstruction.

### **5.3 Comparative Study of Filters**

All the four specimen are examined with five different Hamming filters. The results have summarised in table 5.1 to table 5.4. As it has been discussed earlier that, for real objects the distribution is unknown and the error in reconstruction cannot be calculated

directly. It has been reported earlier that, for a given data set, sharpness can be used as an indicator of the behaviour of error, arising due to the choice of the filter function. The sharpness graphs for the real objects are shown in Fig. 5.1 and Fig. 5.2. The graphs shows a linear relationship with different intercept and slopes.

The theorem which was given by (Munshi [1992]) has been already verified for X-rays (Munshi et al [1993]), (Davis et al [1996]) and for X-rays and gamma rays by (Wells and Munshi [1994]). But for the first time an ultrasonic set of data is used to verify the above theorem.

Filters	NMIN	NMAX	1/NMAX
h51	-78500	194167	$5.10 \times 10^{-6}$
h75	-132802	327632	$3.05 \times 10^{-6}$
h80	-152231	360156	$2.77 \times 10^{-6}$
h91	-197653	436298	$2.28 \times 10^{-6}$
h99	-229768	489627	$2.04 \times 10^{-6}$

Table 5.1: Summary of results for Specimen 1

Filters	NMIN	NMAX	1/NMAX
h51	-5608	107363	$9.31 \times 10^{-6}$
h75	-7733	111917	$8.93 \times 10^{-6}$
h80	-8297	114162	$8.75 \times 10^{-6}$
h91	-12857	120226	$8.31 \times 10^{-6}$
h99	-16431	124398	$8.03 \times 10^{-6}$

Table 5.2: Summary of results for specimen 2

Filters	NMIN	NMAX	1/NMAX
h51	-17324	100811	$9.91 \times 10^{-6}$
h75	-31618	112463	$8.89 \times 10^{-6}$
h80	-35242	115256	$8.67 \times 10^{-6}$
h91	-43686	121892	$8.20 \times 10^{-6}$
h99	-49636	126466	$7.90 \times 10^{-6}$

Table 5.3: Summary of results for specimen 3

Filters	NMIN	NMAX	1/NMAX
h51	-21987	127788	$7.82 \times 10^{-6}$
h75	-33179	149751	$6.67 \times 10^{-6}$
h80	-36475	155561	$6.42 \times 10^{-6}$
h91	-47097	169245	$5.90 \times 10^{-6}$
h99	-55471	178767	$5.59 \times 10^{-6}$

Table 5.4: Summary of results for specimen 4

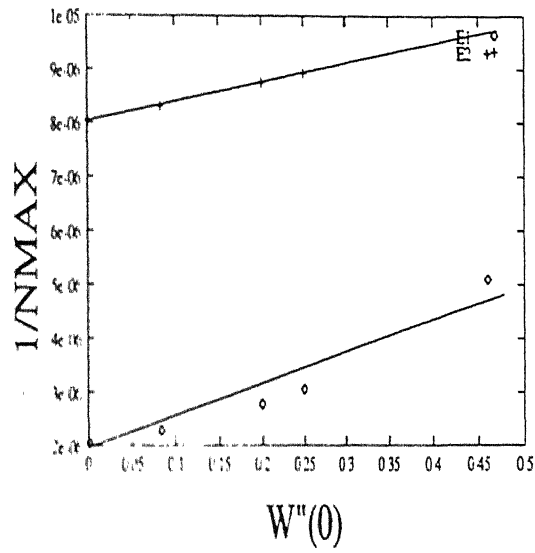


Figure 5.1: 1/NMAX plot for real specimens

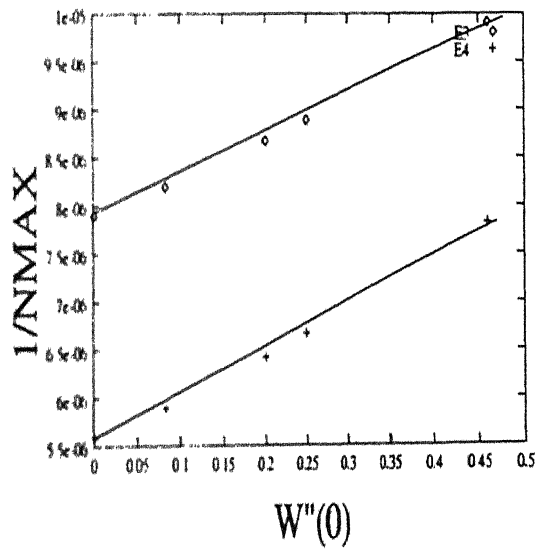


Figure 5.2: 1/NMAX plot for real specimens

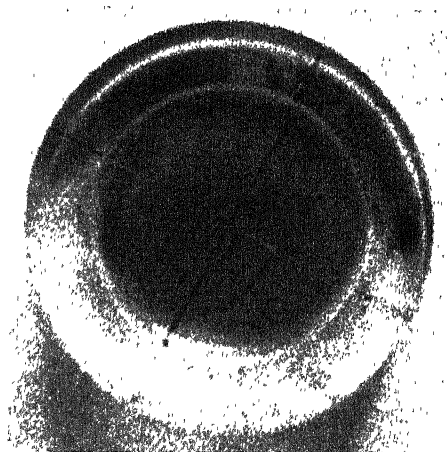
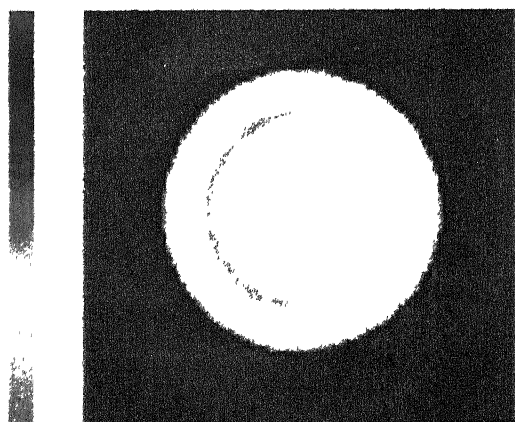
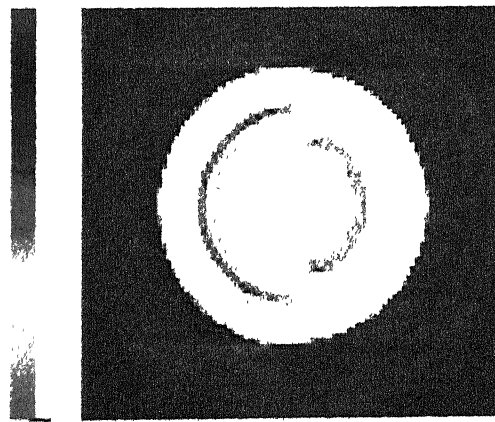


Fig. 5.1: Original Image for the Specimen 1



Min = 20.0000      Max = 225.0000  
 LAvg = 1158.7255    AAvg = 611.4225  
 File : h54.fil, NRay : 90, NView : 90



Min = 1.0000      Max = 256.0000  
 LAvg = 1156.2762    AAvg = 609.4899  
 File : h99.fil, NRay : 90, NView : 90

Fig. 5.2: Reconstructed Image with h54 and h99 filters

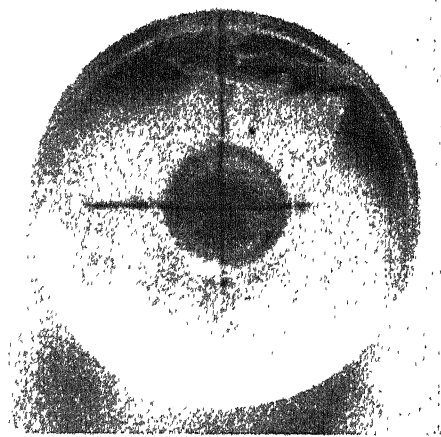
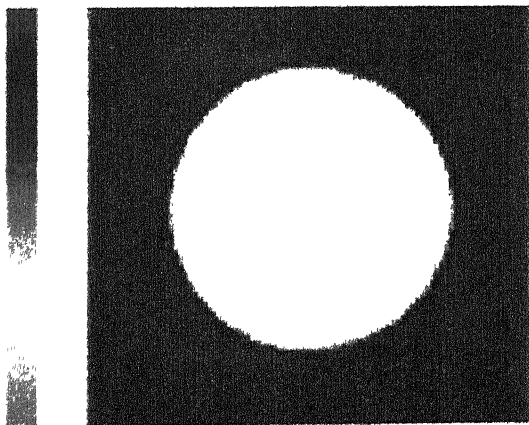
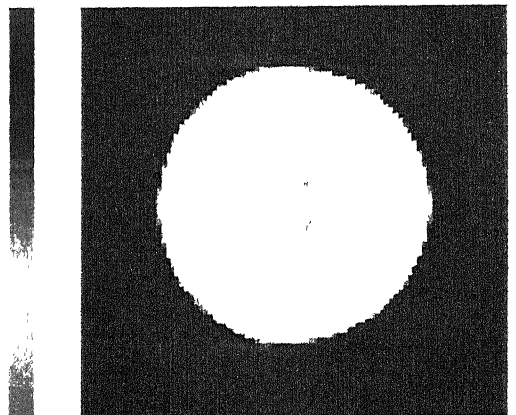


Fig. 5.3: Original Image for the Specimen 2



Min = 21.0000      Max = 216.0000  
 LAvg = 1134.9617    AAvg = 613.9705  
 File : h54.fil, NRay : 90, NView : 90



Min = 1.0000      Max = 256.0000  
 LAvg = 1133.1073    AAvg = 614.8852  
 File : h99.fil, NRay : 90, NView : 90

Fig. 5.4: Reconstructed Image with h54 and h99 filters

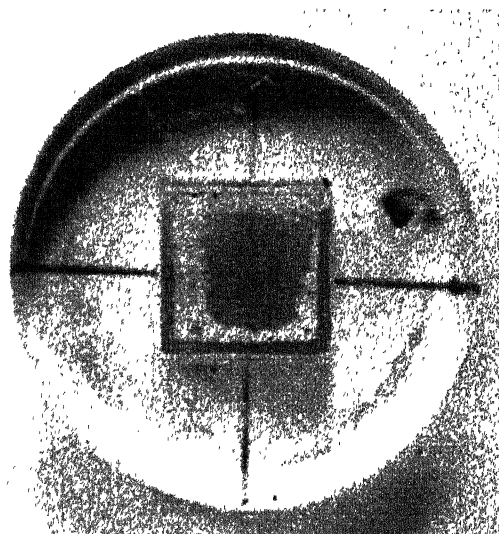
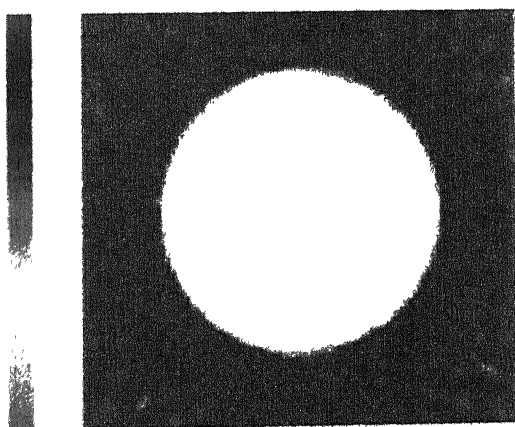
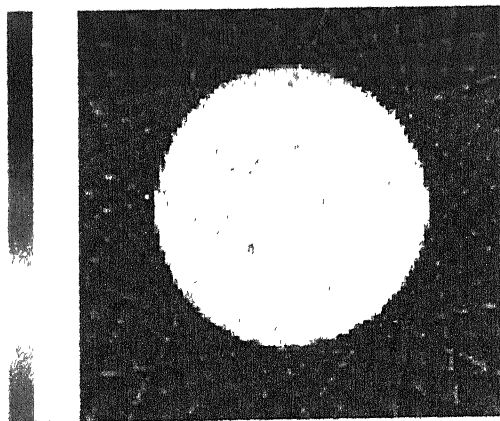


Fig. 5.5: Original Image for the Specimen 3



Min = 47.0000      Max = 218.0000  
 LAvg = 1132.6555    AAvg = 610.8762  
 File : h54.fl, NRay : 90, NView : 20



Min = 1.0000      Max = 256.0000  
 LAvg = 1130.0575    AAvg = 611.4248  
 File : h99.fl, NRay : 90, NView : 20

Fig. 5.6: Reconstructed Image with h54 and h99 filters

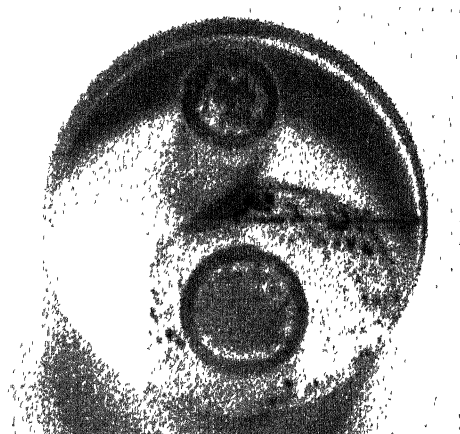
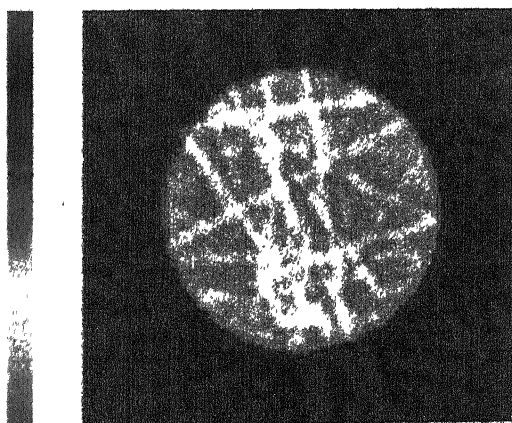
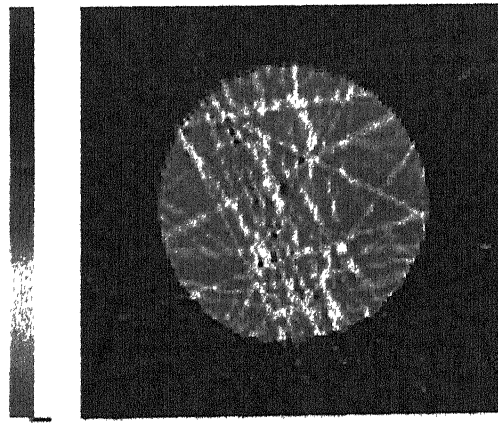


Fig. 5.7: Original Image for the Specimen 4



Min = 37.0000      Max = 200.0000  
 LAvg = 1292.6339    AAvg = 619.1910  
 File : h54.fl, NRay : 90, NVlew : 20



Min = 1.0000      Max = 256.0000  
 LAvg = 1359.5985    AAvg = 619.8182  
 File : h99.fl, NRay : 90, NVlew : 20

Fig. 5.8: Reconstructed Image with h54 and h99 filters

## Chapter 6

# Conclusions and Suggestions for Future Work

From the study of the reconstructed images of the specimens, following conclusion can be drawn

- \* Circular defects at the center with 15 mm or more diameter can be easily detected and sized .
- \* Square defects at the center with size 25 mm x 25 mm or more can be detected but exact sizing cannot be done. In general defects do not have sharp edges as compared to square so defects which are similiar to square can be detected and sized.
- \* Two or more defects of different sizes cannot be detected very easily but in such type of specimen it can be said that there are two different acoustic impedance zones.
- \* The results can further improved if more no of projections with more number of rays are taken and with smaller diameter ultrasonic probes.

## Future Work

- Data can be collected for specimen with small size inclusions of different materials.
- A suitable method should be adopted to remove the wobble in the rotating table of the ultrasonic setup.
- A suitable method should also be adopted to match the center of the rotating table, specimen holder and the specimen.
- Ray tracing can be applied.

## References

- [1] Bray D F and Stanley R K , 1989, *Nondestructive Evaluation*, McGraw-Hill Book Company
- [2] Davis G R , Munshi P , Elliot J C , 1996, An analysis of biological hard tissues using the total least error reconstruction formula, *Journal of X-ray Science and Technology*, vol. 6, pp. 63-76
- [3] Datta D , 1998, *A methodology in ultrasonic NDE for identification and reconstruction of defects in fibre composites* Ph.D. Thesis, Indian Institute of Technology Kanpur
- [4] Hayford D T and Henneke E G II, 1979, A model for correlating damage and attenuation in composites, *Composite Materials: Testing and Design (fifth conference)*, ASTM STP 674, American Society of Testing Materials, Philadelphia, PA, pp. 184-200.
- [5] Herman G T , 1980, *Image reconstruction from projections: The Fundamentals of Computerized Tomography*, Academic Press (New York).
- [6] Hounsfield G N , 1973, Computerized transverse axial scanning tomography, Part I: Description of the system, *British Journal of Radiology*, vol.46, pp. 1016-1022.
- [7] Jansen D P and Hutchins D A , 1992, Immersion Tomography using Rayleigh and Lamb waves, *Ultrasonics* Vol. 30, pp. 245-254

- [8] Jansen D P , Hutchins D.A., Young R P., 1993, Ultrasonic Tomography using Scanned Contact Transducers, *Acoustical Society of America*, Vol. 93, No. 6, pp. 3242-3249.
- [9] Lewitt R M , 1983, Reconstruction algorithms: Transform Methods, *Proceedings IEEE*, Vol. 71, No. 3, pp. 390-408.
- [10] Munshi P , Maisl M , Reiter H., 1997, Experimental aspects of the approximate error formulae for tomographic reconstruction, *Materials Evaluation*, pp. 188-191.
- [11] Munshi P , 1992, Error analysis of tomographic filters – I: Theory, *NDT&E International*, pp. 191-194
- [12] Natterer F , 1986, *The Mathematics of Computerized Tomography*, John Wiley and Sons, New York
- [13] Rogovsky A J , 1985, Ultrasonic and thermographic methods for NDE of composite tubular parts, *Materials Evaluation*, Vol. 43, pp. 547-555.
- [14] Wells P, Munshi P , 1994, An investigation of the theoretical error in tomographic images, *Nuclear Instruments and Methods in Physics Research, B*, pp. 87-92.
- [15] Wright W , Hutchins D., 1997, Air Coupled Lamb Wave Tomography, *IEEE Transactions on Ultrasonics*, Vol. 44, No. 1, pp. 53-59.

TH  
NET/1999/M  
M319u  
A129574

129574

This book is to be returned on the date last stamped.

[illegible]